

Fresnel reflection suppression from deterministic illumination diffusers using antireflection random nanostructures

Praneeth Gadamsetti* and Menelaos K. Poutous

University of North Carolina at Charlotte, Department of Physics and Optical Science, Charlotte, North Carolina, United States

Abstract. Deterministic illumination diffractive-diffusers have nonperiodic short and medium-scale topography. Because of the deterministic locations of vertical sidewalls at the phase transition boundaries, over-coating diffractive diffusers with thin-film antireflection layers perturbs their function, resulting in performance deviations and nonuniformities. To mitigate these effects, we added antireflection random nanostructures on the surface of three different classes of fused-silica multiphase diffractive diffusers, using reactive-ion plasma etching. The diffusers were measured before and after the random nanostructures addition, using a polarized-laser scatterometer with a dynamic range of nine orders of magnitude. The bidirectional scatter distribution function was measured over the entire equatorial plane of incidence, to analyze the directionality of scattered light and the impact of the antireflective nanostructure presence on the optical performance of the diffusers. The overall reflectivity suppression was measured across the illumination patterns directions, as well as, across the entire 180-deg angle-sweep. The designed deterministic illumination patterns and their contrast were unaffected by the presence of the random antireflective structures, whereas Fresnel reflectivity was reduced by an order of magnitude on average. © The Authors. Published by SPIE under a Creative Commons Attribution 4.0 International License. Distribution or reproduction of this work in whole or in part requires full attribution of the original publication, including its DOI. [DOI: [10.1117/1.OE.61.6.063106](https://doi.org/10.1117/1.OE.61.6.063106)]

Keywords: nanostructured surfaces; Fresnel reflection; antireflection structured surface; random structures; deterministic illumination diffusers; bidirectional scatter density function.

Paper 20220290G received Mar. 22, 2022; accepted for publication Jun. 2, 2022; published online Jun. 21, 2022.

1 Introduction

Fresnel reflection is observed when light travels across an interface separating two media with different refractive indices. To enhance the performance of optical multicomponent systems, Fresnel reflections from sequential optical surfaces need to be suppressed. Antireflection thin film coatings are the most prominent technique used to reduce these reflections. In principle, destructive interference between multiple reflections from the top and bottom boundaries of films, caused by the net optical-path induced phase difference, results in phase enhancement in the transmission direction and suppression of reflection. Multilayered thin film coatings are often preferred as an antireflection treatment, due to high-transmission efficiency designs and broad spectral band performance (BBAR), although their fabrication can be complicated due to repetitive multiple-layer depositions. Multilayered AR coatings contain a minimum of two dissimilar materials, which further introduces thermal mismatches and mechanical instability due to deposition-induced stresses in the interfacial regions. BBAR are designed for a specific angle of incidence (AOI) conditions, as the phase difference is optical path-dependent and therefore changes as a function of AOI.

Random antireflective subwavelength surface structures (rARSS) in recent years have been used as a research alternative to conventional thin-film coatings.¹⁻⁵ These columnar nanostructures have random spatial surface distributions, are subwavelength in average cross-section, wavelength-scale in-depth, and are fabricated directly on the substrate's surface. rARSS are

*Address all correspondence to Praneeth Gadamsetti, pgadamse@unc.edu

approximated and numerically modeled, as an effective-medium layer on top of the substrate, reducing reflectance and increasing transmission into the substrate by index-contrast diffusion.⁶ Reports have demonstrated broadband spectral reflectivity suppression, with enhanced transmission for normal and off-normal AOI, and polarization insensitivity.⁷ A variety of rARSS fabrication methods have been investigated to date on various types of substrates. The fabrication methods of the nanostructures can be grouped into two main classifications: bottom-up and top-down. Nanostructures fabricated using bottom-up methods use different additive techniques, such as wet-solution processing or physical or chemical vapor deposition.^{8,9} Fabrication of rARSS has been reported on fused silica, borosilicate glasses, and IR windows, using reactive ion etching (RIE) and inductively coupled plasma etching process, with or without random metallization masks.^{10,11}

Most reported work on rARSS has been limited to planar surfaces, such as optical windows. Fewer reports are available on nonplanar surfaces, such as lenses and binary diffractive gratings.^{12–14} Diffractive optical elements (DOE), such as spot array generators, beam shapers, and controlled-angle illuminators, are optics with surface-encoded phase information, usually generated by iterative-optimization Fourier transform algorithms, to redistribute incident light irradiance and generate a desired radiance pattern in the far-field.^{15,16} DOE have Fresnel losses, and coating them with conformal or nonconformal thin film coatings is challenging due to their complicated surface topography. For a DOE to function as intended, the coatings must be included in the original design specifications, further increasing their complexity.^{17,18} RF-driven ion plasma dry-etching fabrication processes are used to fabricate rARSS. Since plasma etches are subtractive processes, nanostructures can be fabricated on pre-existing DOE topography, and care needs to be taken when applied so that the relative phase depths of the DOE profiles are not perturbed. Such a deviation from the relative phase depths can lead to optical performance inefficiency from the intended design. More specifically, for the controlled-angle diffusers and deterministic DOE, phase errors lead to “parasitic” observable diffraction effects, such as diffraction angle deviation, projection pattern aliasing, and illumination imbalance, such as an increase in zeroth-order diffraction efficiency.¹⁹

Nanostructuring an optical surface requires the introduction of roughness much smaller in scale than the functional application wavelength. Presence of nanoscaled transverse cross-sections of the AR structures can result in nondeterministic scatter in projection space, such as diffuse light, leading to degradation of illumination pattern contrast, which can overwhelm any AR benefits due to the elimination of Fresnel reflectivity. Since a DOE acts as a deterministic scatterer, a high-sensitivity scatterometer can be used to measure the effects of rARSS on component performance. The bidirectional scattering distribution function (BSDF), defined in the radiometric terms as the scattered radiance over incident irradiance, is commonly used to quantify scattered light distributions resulting from the light incident on rough surfaces.^{20,21} Angle-resolved scatter signatures of the DOE, before and after rARSS addition, can be used to compare the on-axis scattering characteristics of nanostructures in transmission as well as reflection.

We present measurements of the diffractive performance of three fused silica, eight-phase level DOE: (a) a narrow-angle, (b) a wide-angle, and (c) a controlled-angle DOE, with 700 nm total etch depth, including rARSS fabricated on the surface of the DOE and on the substrate’s second planar interface (backside). The BSDF and the integrated BSDF on-axis (projection field) and off-axis signatures were measured at 633 nm for *s*-polarized light at normal incidence.

2 Randomly Textured Antireflection Surface Fabrication

Three commercially available, uncoated, multiphase level diffractive diffusers on a fused silica substrate were chosen to study the effects of rARSS in addition to their profiles. The DOE has different feature sizes and design complexity, from large to small phase-step profiles, and with narrow quasioone-dimensional (1D) structures as shown in Fig. 1. The narrow-angle DOE [Fig. 1(a)] was designed to perform as a two-dimensional (2D) spot array generator of 11×7 spots, with a narrow projected field of ± 1 deg. Distinguishable deterministic light scatter is observed within a field of view of ± 5 deg, as undesired diffraction orders appear in addition to the designed pattern intensity distribution, due to constraints such as unit cell periodicity and

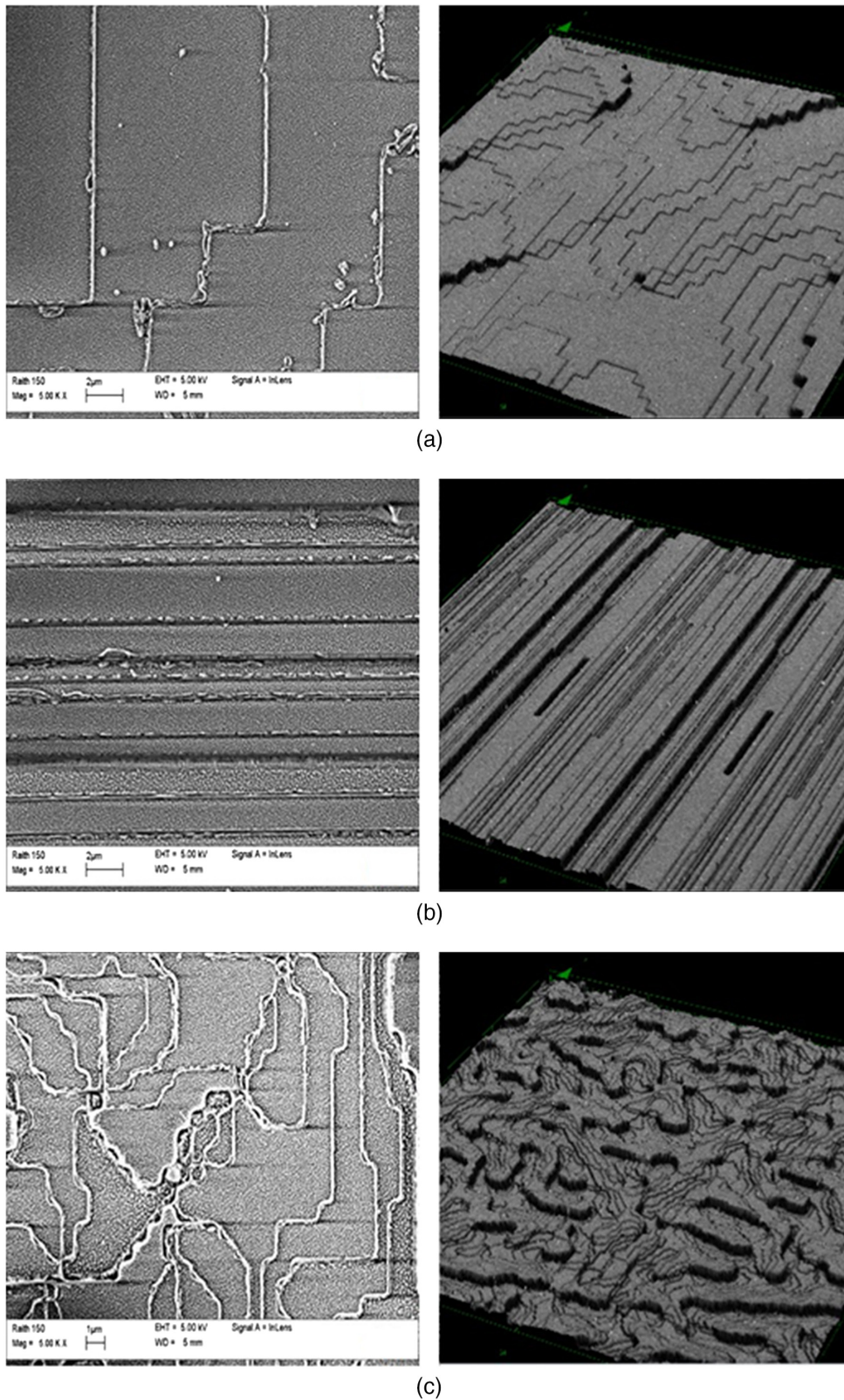


Fig. 1 Top-down SEMs (on the left) and UV-confocal microscope stereoscopic images (on the right) of the three multiphase DOEs where rARSS have been added. The transverse boundaries are phase transitions between different phase levels that are populated by nanostructures. (a) Narrow-angle 2D spot array diffuser, (b) wide-angle 1D spot array diffuser, and (c) controlled-angle diffuser.

phase profile segmentation. The wide-angle DOE [Fig. 1(b)] was designed to perform as a 1D (line) spot array generator of 1×13 spots with a wide projected field angle of ± 5 deg. The controlled angle DOE [Fig. 1(c)] performs as an off-axis segmented annulus projector, with distinguishable zeroth-order at the center of the projected field angle of ± 5 deg.

The prefabricated fused silica DOE was immersed in ethanol for 10 min, followed by drying with flowing nitrogen gas. A magnetron sputtering deposition tool (AJA 1800-F) was used to deposit a thin discontinuous layer of Au (< 20 nm) on the backside of the DOE, and the substrate was etched by a reactive-ion plasma gas mixture of sulfur-hexafluoride (SF_6), and oxygen (O_2). The rARSS fabrication process parameters were previously optimized for fused silica optical windows, to maximize reflectivity suppression at the incident wavelength of 633 nm.¹⁰ An Surface Technology Systems (STS) advanced oxide etcher was used, setting the platen power at 60 W, the SF_6 flow rate at 50 sccm, the O_2 flow rate at 5 sccm, chamber pressure at 24 mT, platen temperature at 20°C, and the total process etch time to 25 min. All DOEs were placed in the chamber together to minimize variations due to serial processing. The thin nonuniform layer of Au facilitates the initiation of the random etch process, and it is eventually removed by the ballistic action of the nonreactive molecular species bombardment throughout the process. The full process was repeated on the front side of the DOE using etching parameters identical to that of the back (flat) surface, to evaluate the rARSS effects without prior special optimization.

Scanning electron microscope (SEM) images of the postprocessed DOE images show the formation of rARSS on the original stepped phase topography, shown in Fig. 1. Uniform formation of nanostructures on all phase levels throughout the surface for the three DOE was observed. Fabrication of random nanostructures on the surface does not show any detrimental effects on the phase features of the DOE, except that edge distortions on the side walls of the phase stepped features was observed. These phase boundary effects are due to reactive plasma action, partially etching the side walls during the fabrication of the nanostructures.²² Any alterations of the DOE transverse feature size and longitudinal phase depth should result in measurable variations of the designed projection patterns and full-field scatter signatures in transmission and reflection. Measurements of these perturbations can give insight into possible undesirable effects of the rARSS on the original DOE profile.

3 Results and Discussion

To measure the performance of the DOE, we employed a scatterometer (CASI[®], Schmitt Industries Inc., Portland, Oregon, USA), with a layout shown in Fig. 2. The scatterometer uses a He:Ne (633 nm) laser source, with an adjustable sample mount for the various AOI, and

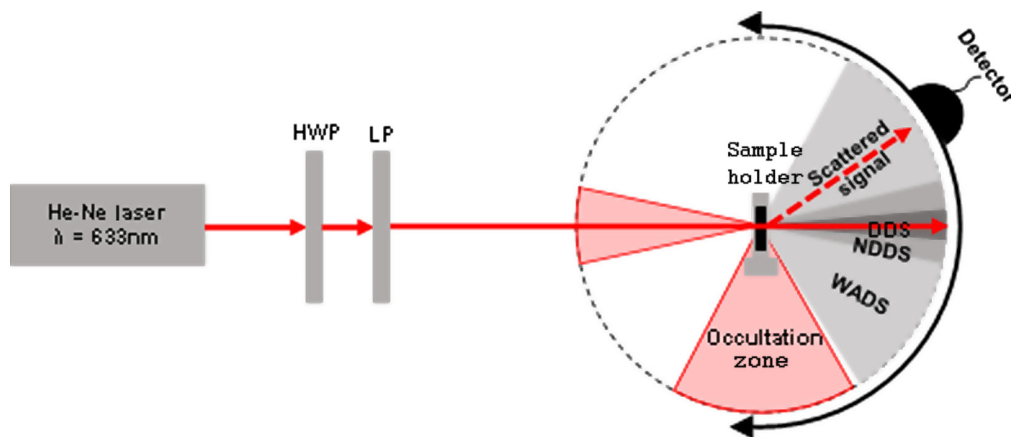


Fig. 2 CASI scatterometer layout. Laser light is directed toward the sample located at the center of rotation of the apparatus, with the detector scanning over the equatorial plane of the unit sphere. HWP is a half-wave plate, LP is the linear polarizer incidence selector, DDS is the deterministic design spot angular range, NDDS is near design deterministic scatter angular region, and WADS is wide-angle deterministic scatter angular region.

Table 1 Integrated transmission scatter intensity for the original diffusers (blank) and the rARSS postfabrication diffusers in design (DDS) and near design specular (NDDS) AOC.

DOE	DDS			NDDS		
	Blank (sr ⁻¹)	rARSS (sr ⁻¹)	Enhancement fraction	Blank (sr ⁻¹)	rARSS (sr ⁻¹)	Enhancement fraction
A	4.71(10 ⁵)	5.00(10 ⁵)	1.06	3.50(10 ³)	3.26(10 ³)	0.918
B	4.35(10 ⁵)	3.74(10 ⁵)	0.86	–	–	–
C	3.80(10 ⁴)	6.66(10 ⁴)	1.74	4.70(10 ³)	4.20(10 ³)	0.885

Table 2 Integrated transmission and reflection scatter intensity for the original diffusers (blank) and the rARSS postfabrication diffusers in wide-angle deterministic scatter (WADS) AOC.

DOE	Transmission			Reflection		
	Blank (sr ⁻¹)	rARSS (sr ⁻¹)	Enhancement fraction	Blank (sr ⁻¹)	rARSS (sr ⁻¹)	Enhancement fraction
A	90.0	1.27(10 ²)	1.47	6.90	1.42	0.204
B	5.70(10 ³)	1.02(10 ⁴)	1.78	2.40(10 ³)	3.55(10 ²)	0.147
C	51.0	65.0	1.28	12.0	1.40	0.115

a motorized detector arm capable of full field scans in transmission and reflection. The instrument is capable of measurements at *s* (TM), *p* (TE), and cross polarization settings and is equipped with focusing optics and detector varying apertures, calibrated to measure high-resolution scans with a dynamic range of over eight-orders in magnitude. The large dynamic range of the scatterometer results in high-valued measured integrated scatter, as shown in Tables 1 and 2. The BSDF is defined as a differential ratio of measured radiance to incident irradiance in units of inverse steradians (sr⁻¹) as

$$BSDF \equiv \frac{dL_c(\theta_c, \varphi_c; \theta_i, \varphi_i)}{dE_i(\theta_i, \varphi_i)} \approx \frac{P_c}{P_i \cos \theta_c} \Delta\Omega_c, \tag{1}$$

where *dL_c*, *dE_i* define the collected differential radiance and incident irradiance; *P_c*, *P_i* are the radiant power (from the surface) and incident power on the scattering surface, respectively. The angular variables *θ_c*, *φ_c*, *θ_i*, *φ_i* correspond to the scattered and incident angles, and *ΔΩ_c* is the solid angle of collection subtended by the detector’s aperture.

The DOE was tested at normal AOI, as per their application specifications, and since no polarization-sensitive behavior was observed, all measurements presented in this report are for the *s* polarization state, which is perpendicular to the plane of incidence shown in Fig. 2. To differentiate between deterministic and random scatter, we include below a short description of the functionality of the DOE diffusers.

Projection of a specific illumination intensity pattern in the near- or far-field can be achieved using DOEs. Such DOE is usually referred to as *diffusive-phase illuminators*. The radiance pattern is designed by numerically perturbing the optical phase of a wavefront, to induce the corresponding diffraction pattern at the desired distance from the optical element. As previously mentioned, the DOE design process consists of numerical optimization iterations of a candidate phase profile and the comparison of the Fresnel (or Fourier) transforms of the profile with the desired intensity spatial distribution, leading to an incremental diffusion to the desired optical phase distribution. There are numerous adaptive or error-reduction algorithms that have been shown to achieve different levels of fidelity for different desired patterns.²³ Sampling and quantization of the phase profile are restricted by fabrication methods, especially transverse-feature

resolution (DOE-plane structure and sampling) and microrelief height (phase quantization). These restrictions lead to deviations from the designed (computed) profile and result in illumination pattern changes. Any implementation issues, due to the inability to achieve a fabrication process to structure the specified phase profile, further impact DOE performance. For a prefabricated DOE illumination diffuser, it is therefore imperative to preserve the lateral (x - y) and longitudinal (h) morphology of the surface through subsequent processing steps, such as AR thin-film coating deposition or rARSS nanostructuring. Process-induced height deviations of the DOE profile affect the efficiency of the illumination distribution, whereas transverse feature erosion or dilation changes the radiance distribution. The later increases the undesirable non-deterministic scatter, where the former imbalances the intensity within the projected pattern. In general, the fabricated DOE phase profile $\Phi(x_m, y_l, h_{ml})$ can have the form

$$\Phi(x_m, y_l, h_{ml}) = \left[\left[\overline{\phi}(x_m, y_l; p_x, p_y, h_{ml}) \Pi\left(\frac{x}{c_x}, \frac{y}{c_y}\right) \right] * \text{III}\left(\frac{x}{c_x}, \frac{y}{c_y}\right) \right] \left(\Pi\left(\frac{x}{N_x c_x}, \frac{y}{N_y c_y}\right) \right), \quad (2)$$

where m, l are the DOE xy -plane pixel indices, $\overline{\phi}(x_m, y_l, h_{ml})$ is the pixelated quantized phase profile for p_x by p_y pixel size, $\Pi(x/c_x, y/c_y)$ is the rectangular DOE region that defines the phase unit cell, $\text{III}(x/c_x, y/c_y)$ is the unit cell replication comb (tiling), $\Pi(x/N_x c_x, y/N_y c_y)$ is the entire DOE window comprising of N -tiled unit cells, and $*$ indicates the convolution operation. The far-field diffraction intensity pattern of such phase profile is

$$I\left(\frac{\sin \alpha}{\lambda}, \frac{\sin \beta}{\lambda}\right) = \left| K_o \left[\overline{F}\left[\left(\frac{\sin \alpha}{\lambda}, \frac{\sin \beta}{\lambda}\right) * \text{sinc}\left(c_x \frac{\sin \alpha}{\lambda}, c_y \frac{\sin \beta}{\lambda}\right) \right] \text{III}\left(c_x \frac{\sin \alpha}{\lambda}, c_y \frac{\sin \beta}{\lambda}\right) \right] * \left(\text{sinc}\left(N_x c_x \frac{\sin \alpha}{\lambda}, N_y c_y \frac{\sin \beta}{\lambda}\right) \right) \right|^2 \quad (3)$$

For α, β , the planar diffraction angles measured from the DOE surface normal, $\overline{F}(\xi, \psi)$ is the Fourier transform of the DOE phase profile, λ is the wavelength of the incident light, and $\text{sinc}(z)$ is the conventional notation for the ratio $\sin(z)/z$. The diffraction intensity is expressed using angular variables to relate to directional scatter angular measurements. Equation (3) restricts the relations between the physical size of the smallest phase pixel (p_x, p_y), the size of the unit cell (c_x, c_y), and the total spatial extent of the DOE ($N_x c_x, N_y c_y$). For a DOE that generates an illumination array of spots, such as the narrow-angle 2D rectangular spot array of Fig. 1(a), each spot has to be separated by one diffraction order at a minimum, to resolve the separation between the spots in the array. The inset in Fig. 3 shows graphically a rectangular spot array. The diffraction order separation is controlled by the phase unit-cell sizes (c_x, c_y). The line-shape (point-spread function) of each diffraction order is determined by the total number of cells repeated within the actively illuminated surface of the entire DOE ($N_x c_x, N_y c_y$). This is readily shown in Fig. 4(b), where 15-diffraction orders are distributed uniformly across a ± 5 deg cone, each having a full-width line-shape of about 0.5 deg. Lastly, diffraction from each phase pixel (p_x, p_y) will result in the bounding envelope of the angularly distributed intensity. To suppress the duplicated diffraction patterns arising from the tiling of the unit-cell, the first null of the diffraction envelop is chosen at or near the boundary of the full diffraction cone. The subsidiary peaks of the point-spread function of the phase pixel dimensions scale the duplicate diffraction patterns. As expected, the relation between the DOE scales is: $p < c < Nc$, and the diffracted angular separations are reciprocal: $p^{-1} > c^{-1} > (Nc)^{-1}$. Any disturbance or perturbation of the scale relations mentioned above will result in parasitic orders between the desired choices, or possible reduction of the original efficiency for each order. Etching the DOE existing profile to induce the rARSS nanoscale distribution should not have such undesirable effects. If we consider that the rARSS feature scales could be less than p_x, p_y by at least an average factor of 100, the nanostructures can at an extreme case induce a nondeterministic scattered redistribution of the projected intensity (halo), which will reduce the transmission contrast performance of the DOE.

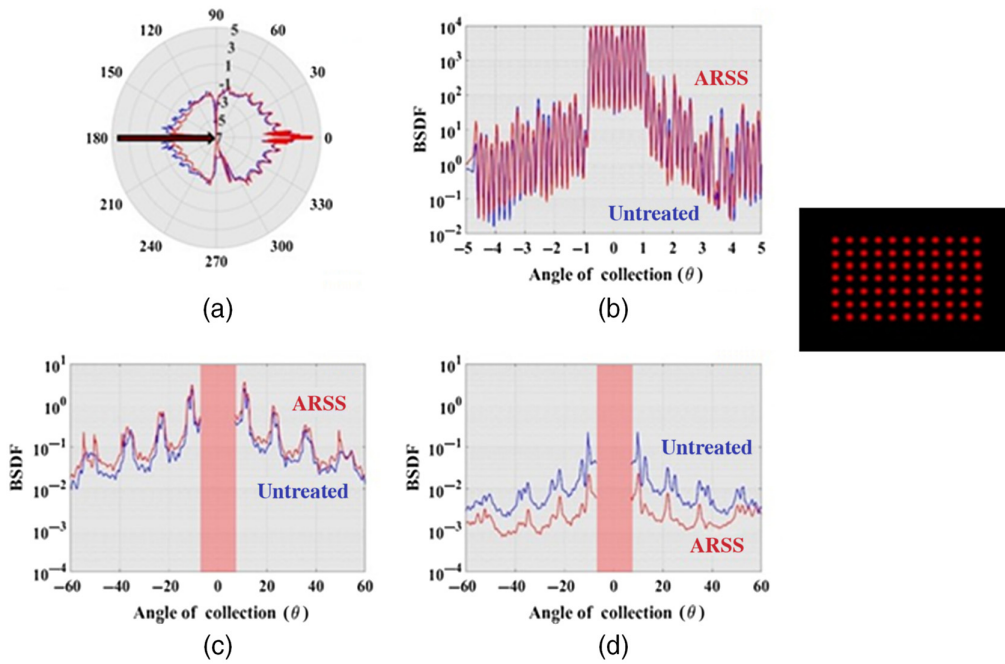


Fig. 3 CASI scatter measurement (BSDF) of narrow-angle diffuser (2D spot array illumination pattern on the right). (a) Full-polar plot of tested DOE. The DOE to be tested is located at the center of circle. The incident light direction is shown with a dark arrow. (b) Limited angle (± 5 deg) along the equatorial axis of transmission of the DOE, (c) measured transmission excluding the ± 5 deg values. (d) Measured reflection excluding the ± 5 deg values. The ± 5 deg FOV (DDS + NDDS region), indicated as a shaded band region, has been removed from the plots (c) and (d) for clarity.

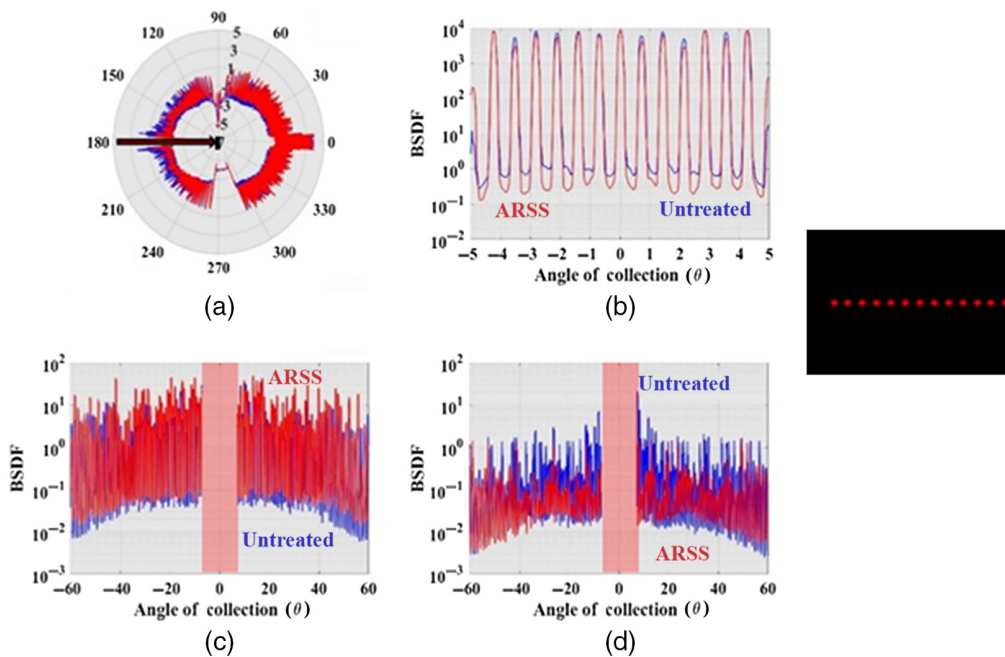


Fig. 4 CASI scatter measurement (BSDF) of wide-angle diffuser (1D spot array illumination pattern on the right). (a) Full-polar plot of tested DOE. The DOE to be tested is located at the center of circle. The incident light direction is shown with a dark arrow. (b) Limited angle (± 5 deg) along the equatorial axis of transmission of the DOE, (c) measured transmission excluding the ± 5 deg values. (d) Measured reflection excluding the ± 5 deg values. The ± 5 deg FOV (DDS + NDDS region), indicated as a shaded band region, has been removed from the plots (c) and (d) for clarity.

We note that Fresnel reflection will induce the same diffraction pattern, although much less intense, which will travel to the back surface of the substrate, where upon a second reflection it will return to the DOE surface and multiplex the transmitted pattern.

To verify the suppression of Fresnel reflectivity by the addition of rARSS, scatter signatures of the unprocessed and rARSS-processed DOE were measured in transmission and reflection. Summing the total transmission and reflection scatter distribution in nondeterministic angles of collection (AOC), equivalent to the total integrated scatter, indicates an overall transmission enhancement and reflection suppression for all the DOE types tested, whereas no significant transmission enhancement was measured along the deterministic projection field of view. In conjunction, because the cross-sectional feature sizes of the nanostructures are 10 to 15 times smaller than the test wavelength, no distinguishable redistributed scatter was observed in off-specular deterministic directions, with the scatter signatures being nearly identical for unprocessed and processed DOE.

A perfectly matched AR coating (PAR) on both surfaces of a fused silica optical window can yield a relative transmission of $(1/0.93 \approx 1.075)$ and relative reflectivity of $(0/0.07 \approx 0)$ at 633-nm wavelength. Where relative transmission is the ratio of absolute maximum transmission values for the PAR fused silica window to the blank fused silica window, and relative reflectivity is the ratio of absolute minimum reflectivity values of the PAR fused silica window to the blank fused silica window. To compare the measured transmission and reflection of the unprocessed and rARSS-processed DOE, the data was segregated into three parts: (a) the deterministic design region (DDS) for an AOC range of $-1 \text{ deg} \leq \theta \leq +1 \text{ deg}$; (b) the near-angle deterministic scatter (NDDS) for an AOC range of $-5 \text{ deg} \leq \theta \leq -1 \text{ deg}$ and $+1 \text{ deg} \leq \theta \leq +5 \text{ deg}$ (excluding the design angular region); and (c) the wide-angle deterministic scatter region (WADS) for an AOC range of $-65 \text{ deg} \leq \theta \leq -5 \text{ deg}$ and $+5 \text{ deg} \leq \theta \leq +65 \text{ deg}$, excluding both previous scatter angular regions. These regions are illustrated as shaded in Fig. 2.

Table 1 lists the angle-integrated normalized transmission of unprocessed and processed DOE and the relative transmission enhancement, defined as the ratio of processed over unprocessed angle-integrated transmission in DDS and NDDS regions. The three tested DOE are listed as samples: A for the narrow-angle 2D spot array, B for the wide-angle 1D spot array and, C for the controlled angle diffuser. They show disparate results with a slight enhancement in transmission for A in DDS and loss in NDDS region (Fig. 3), whereas for B a loss was observed in DDS and NDDS region (Fig. 4). For C, a disproportionate enhancement for the zeroth-order in DDS and loss in NDDS region were measured (Fig. 5).

Table 2 lists the angle-integrated normalized transmission and reflection, and relative transmission enhancement and reflection suppression, for the unprocessed and processed WADS region. Unlike the DDS and NDDS regions, a clear enhancement in transmission and suppression in reflection was measured for all DOE. For the 2D spot array (A) and 1D spot array DOE (B), almost half an order of magnitude in transmission enhancement was observed, compared with the controlled angle diffuser (C), which is only a quarter of an order in magnitude. In reflection, a consistent suppression of an order of magnitude was measured in all cases. The deviation in results for the WADS compared with DDS and NDDS regions could be attributed to phase depth errors due to the subtractive nature of the etching process employed for the fabrication of rARSS on the surface of DOE and not due to the presence of rARSS.

To compare rARSS effects in transmission and reflection of the deterministic radiance profiles, measured scatter scans pre- and post-etch are shown in the entire equatorial plane in Figs. 3–5. Angular radiance replicas were detected for all DOE, due to their respective periodic unit cells. It is evident from the polar plots of the DOE scatter signatures that the addition of rARSS has not perturbed the wide-angle deterministic scatter, and the periodic replicas, which are nonzero due to the finite numerical optimization residuals, are clearly distinguishable at wide AOC. In Fig. 3(b), the narrow-angle 2D spot array radiance within the designed axial deflection angle $\pm 1 \text{ deg}$, displays no major deviations in uniformity, contrast, and spot sizes, between before and after the nanostructures addition. In contrast, the wide-angle spot array as shown in Fig. 4(b), which has diffractive feature sizes and sharp phase transitions compared with the narrow-angle diffuser, show significant effects of nonuniformity and increased contrast after rARSS addition, for all projected spots, even though the transverse spot sizes have remained unperturbed.

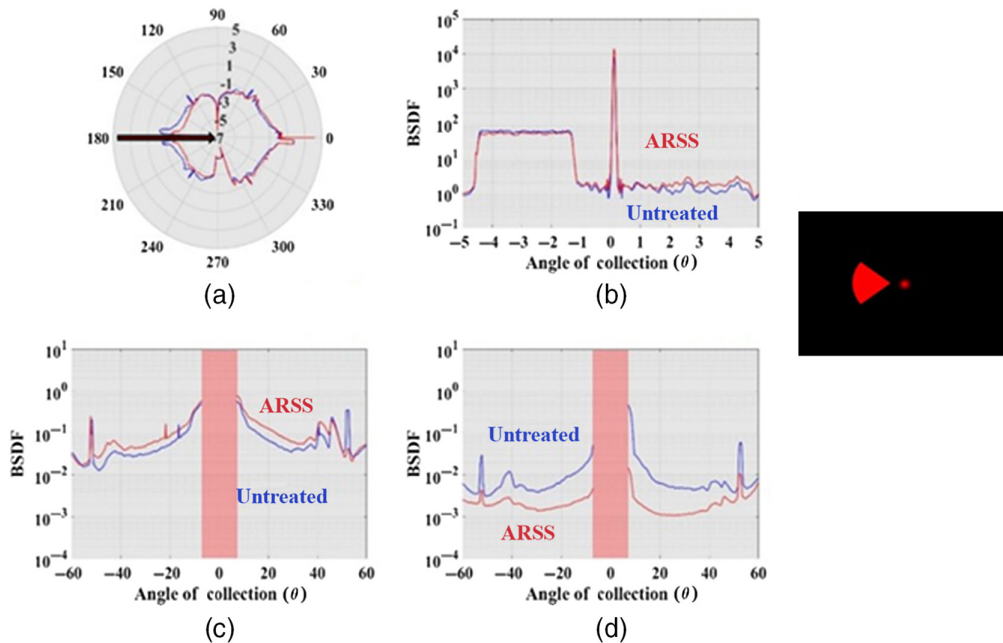


Fig. 5 CASI scatter measurement (BSDF) of controlled angle diffuser (illumination pattern on the right). (a) Full-polar plot of tested DOE. The DOE to be tested is located at the center of circle. The incident light direction is shown with a dark arrow. (b) Limited angle (± 5 deg) along the equatorial axis of transmission of the DOE, (c) measured transmission excluding the ± 5 deg values. (d) Measured reflection excluding the ± 5 deg values. The ± 5 deg FOV, indicated as a shaded band region, has been removed from the plots (c) and (d) for clarity.

At large AOC, rARSS enhanced wide-angle diffuser (C) is not as effective in suppressing reflection, compared with the narrow-angle diffuser (B), as shown in Figs. 4(d) and 3(d). The controlled angle diffuser C has a more complex topographic phase profile compared with the other two DOE (Fig. 1), and its transverse feature size dimensions are smaller than the features of A, but larger than the features in B. For C, the measured reflection and transmission at wide-AOC has similar performance between the original and rARSS-inclusive elements [Figs. 5(c) and 5(d)]. A considerable increase in the zeroth-diffraction order intensity was measured for the controlled angle diffuser post-rARSS addition, which indicates an overall DOE phase imbalance, due to postetching perturbations of the relative depths of the DOE surface [Fig. 5(b)].

Scatter measurements of the postfabrication rARSS on the DOE compared with the unprocessed originals show some changes in performance. To investigate further, we employed granulometry to study the transverse cross-section distributions of the rARSS nanostructures. Since the structures have small cross-sectional dimensions, mechanical contact profile and microscope measurements cannot resolve their structure. Granulometry is a numerical processing technique used to identify the boundaries and define scaled structure elements on images.^{7,24} Top-down high-resolution SEM micrographs were obtained to calculate the normalized granule pattern spectra $\varphi(k)$, for both islands and voids of diameter k . The granule pattern spectra correspond to the discrete probability distribution function of the respective feature size bound by the condition

$$\varphi_{\text{islands}}(k) + \varphi_{\text{voids}}(k) \leq 1. \quad (4)$$

The equality is true only for $k = \infty$, i.e., when all the feature diameters are counted, and a balance of the islands and voids is obtained for each SEM image. The DOE tested has by design varying topographies and three-dimensional feature sizes, independent of the nanostructures. To verify the effects of the surface topography by the subtractive fabrication process, we computed the discrete probability distribution function of rARSS on the witness flats and DOE from sample SEM images. The measured histograms, shown in Fig. 6, show similar island distributions, with feature size mean values of about 50 nm. The distributed histograms of voids are similar for

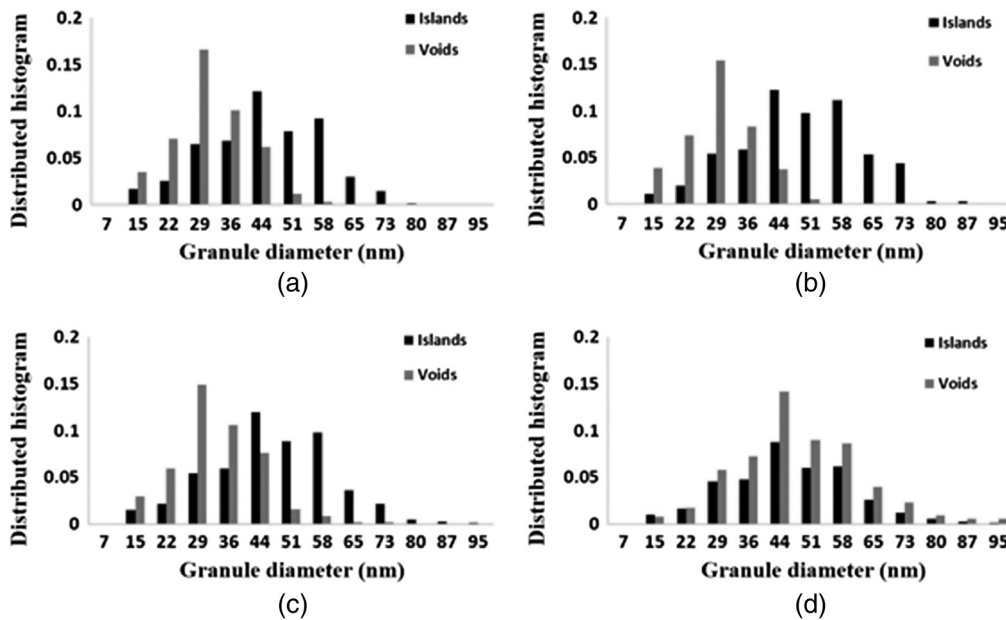


Fig. 6 Distributed histograms of the islands (black) and voids (gray) measured using granulometry (a) witness optical window, (b) narrow-angle diffuser (2D spot array: A), (c) wide-angle diffuser (1D spot array: B), and (d) controlled angle diffuser (C).

all tested surfaces, except that of the controlled angle diffuser. A significant deviation of the void-size peak value was detected for the controlled angle diffuser C (43.6 nm), when compared with the flat witness or the other two DOE corresponding void peak values of 29.1 nm. The measured cumulative distribution of the islands for the witness, narrow-angle diffuser (A), and wide-angle diffuser (B) was calculated to be $\sim 51\%$, whereas for the controlled angle diffuser (C) is 40%, indicating differences in the density of the nanostructures fabricated on the surface. The variations in the distributed histograms and cumulative distributions of rARSS signify differences in fabrication process equilibrium as a function of the DOE existing phase-surface topography.

4 Conclusions

The performance of the random antireflection subwavelength surface structures fabricated on the three different classes of fused silica deterministic DOE was measured using a scatterometer at 633 nm. The antireflective nanostructures were fabricated using a two-step process, with an initial masking step followed by reactive-ion plasma etching. The measured bidirectional scatter distribution functions of the rARSS-processed DOE show similar signatures compared with unprocessed DOE of the same design, with the individual periodic replicas and off-target design deterministic scatter remaining unaltered by the presence of the nanostructures.

The measured integrated wide-angle deterministic scatter intensities of the DOE with rARSS show an order of magnitude suppression in reflectivity compared with the original performance. The measured integrated deterministic design spot scatter transmission intensities show an enhancement for the narrow-angle and controlled angle diffusers, and a loss was observed for the wide-angle diffuser post fabrication. A consistent enhancement in wide-angle deterministic scatter intensities was observed for all DOE. Due to the measured disparities, in transmission enhancement and reflectivity suppression for wide-angle deterministic scatter, compared with the deterministic design spot and near design deterministic scatter, the scatter was analyzed for any detectable addition of diffuse light due to the presence of rARSS. For the designed illumination patterns, DOE with large spatial features, such as the narrow-angle diffuser (2D spot array A), show no deviations, whereas the wide-angle diffuser (1D spot array B) shows an increase in nonuniformity. Significant increase in the zeroth-diffraction order (on-axis) was observed for the controlled angle diffuser C. Even though differences in the design illumination pattern were observed, no distinguishable nondeterministic scatter was observed, with the design target spot

sizes and contrast of the illumination spots and radiance copies remaining unperturbed. These results suggest that variations in the performance of the DOE post-rARSS fabrication are due to relative phase depth erosion induced by the etching process.

The cause of performance deviations between A, B, and C DOE, appears to be due to their dissimilar surface topography interaction with the formation of the rARSS. We employed granulometry to measure the population distributions of the fabricated nanostructures on each DOE. The distribution histograms of the islands on the various DOE topography showed no significant deviations when compared with rARSS fabricated on a flat optical window witness sample. Differences in the cumulative granule distributions of islands and voids signify dependence of the rARSS formation on the surface topography. Even though large differences were not observed in the distribution histograms, a noticeable difference in the average lateral feature size of the voids on diffuser C was observed. The results suggest that, although different surface topographies lead to different rARSS fabrication process-equilibrium conditions, Fresnel reflectivity is successfully suppressed by a factor of 5 to 8 times (Table 2), for wide-angle deterministic scatter. Therefore, random antireflection nanostructures can be employed as an effective reflectivity suppression treatment, for a variety of existing DOE, without compromising their original functionality.

Acknowledgments

The authors would like to acknowledge facilities and equipment support from the Department of Physics and Optical Science and the Center of Optoelectronics and Optical Communications at the University of North Carolina at Charlotte. An earlier version of some results shown in this paper was presented and published under Praneeth Gadamsetti, Karteek Kunala, Menelaos K. Poutous, "Random anti-reflection subwavelength surface structures on deterministic illumination diffusers," Proc. SPIE 11694, Photonic and Phononic Properties of Engineered Nanostructures XI, 1169416 (5 March 2021); <https://doi.org/10.1117/12.2577040>.

References

1. Q. Yang et al., "Antireflection effects at nanostructured material interfaces and the suppression of thin-film interference," *Nanotechnology* **24**(23), 235202 (2013).
2. S. Chattopadhyay et al., "Anti-reflecting and photonic nanostructures," *Mater. Sci. Eng.: R: Rep.* **69**, 1–35 (2010).
3. D. S. Hobbs, B. D. MacLeod, and J. R. Riccobono, "Update on the development of high performance anti-reflecting surface relief micro-structures," *Proc. SPIE* **6545**, 65450Y (2007).
4. L. E. Busse et al., "Anti-reflective surface structures for spinel ceramics and fused silica windows, lenses and optical fibers," *Opt. Mater. Express* **4**(12), 2504–2515 (2014).
5. D. Vandormael et al., "Anti-reflective sub-wavelength patterning of IR optics," *Proc. SPIE* **6395**, 63950L (2006).
6. C.-H. Chang et al., "Nanostructured gradient-index antireflection diffractive optics," *Opt. Lett.* **36**(12), 2354–2356 (2011).
7. A. E. Peltier et al., "Polarization insensitive performance of randomly structured antireflecting planar surfaces," *Opt. Eng.* **57**(3), 037109 (2018).
8. U. Schulz et al., "Antireflection of transparent polymers by advanced plasma etching procedures," *Opt. Express* **15**(20), 13108–13113 (2007).
9. U. Schulz et al., "Gradient index antireflection coatings on glass containing plasma-etched organic layers," *Opt. Mater. Express* **5**(6), 1259–1265 (2015).
10. A. P. Eckart et al., "Control of spectral transmission enhancement properties of random anti-reflecting surface structures fabricated using gold masking," *Proc. SPIE* **10115**, 101150B (2017).
11. B. Zollars et al., "Performance measurements of infrared windows with surface structures providing broadband wide-angle antireflective properties," *Proc. SPIE* **8708**, 87080Q (2013).

12. C.D. Taylor, "Optical performance of random anti-reflection structured surfaces (rARSS) on spherical lenses," Doctoral Dissertation, University of North Carolina at Charlotte (2016).
13. C. Pacholski et al., "Antireflective subwavelength structures on microlens arrays—comparison of various manufacturing techniques," *Appl. Opt.* **51**(1), 8–14 (2012).
14. K. Kunala and M. K. Poutous, "Diffraction efficiency performance of random anti-reflecting subwavelength surface structures on prefabricated fused silica binary gratings," *Appl. Opt.* **57**(16), 4421–4427 (2018).
15. L. De Sio et al., "Beam shaping diffractive wave plates," *Appl. Opt.* **57**(1), A118–A121 (2018).
16. M. D. Himel et al., "Microfabrication of controlled angle diffusers used for resolution enhancement in microlithography," *Proc. SPIE* **4984**, 1–9 (2003).
17. A. A. Cruz-Cabrera, "Fabricating surface-relief diffractive optical elements," in *Microoptics and Nanooptics Fabrication*, S. A. Kemme, Ed., pp. 1–38, CRC Press, Boca Raton, Florida (2010).
18. M. D. Himel et al., "Design and fabrication of customized illumination patterns for low-k1 lithography: a diffractive approach," *Proc. SPIE* **4346**, 1436–1442 (2001).
19. V. Kettunen et al., "Diffractive elements designed to suppress unwanted zeroth order due to surface depth error," *J. Mod. Opt.* **51**(14), 2111–2123 (2004).
20. P. Gadamsetti, K. Kunala, and M. K. Poutous, "Optical scattering measurements of random anti-reflection subwavelength surface structures on binary gratings," *Proc. SPIE* **11276**, 1127619 (2020).
21. J. C. Stover, *Optical Scattering: Measurements and Analysis*, 3rd ed., SPIE Press, Bellingham, Washington (2012).
22. K. Kunala and M. K. Poutous, "Random antireflective nanostructuring on binary near-wavelength period gratings," *Opt. Eng.* **57**(8), 087106 (2018).
23. V. A. Soifer, *Methods for Computer Design of Diffractive Optical Elements*, John & Sons, Inc., New York (2002).
24. E. R. Dougherty and R. A. Lotufo, *Hands-on Morphological Image Processing*, SPIE Press, Bellingham, Washington (2003).

Praneeth Gadamsetti is a doctoral candidate in the Optical Science and Engineering Program at UNC Charlotte. His research efforts include the fabrication of micro-optical elements, random antireflective subwavelength structures (rARSS), optical performance, and surface scatter characterization.

Menelaos K. Poutous received his doctorate degree from the School of Physics at the Georgia Institute of Technology in 1996. He is an associate professor in the Department of Physics and Optical Science at UNC Charlotte. He previously held a principal development engineer's position at Digital Optics Corporation, and before that, he was a physics lecturer at Emory University. His research interests are in spectroscopy, diffractive micro-optical elements, photolithographic microfabrication, and artificial optical surfaces.